Chemical Science

ROYAL SOCIETY OF CHEMISTRY

EDGE ARTICLE

View Article Online
View Journal | View Issue

Cite this: *Chem. Sci.*, 2025, **16**, 11989

All publication charges for this article have been paid for by the Royal Society of Chemistry

Steric hindrance modulated efficient thermally activated delayed fluorescence with non-linear optical, ferroelectric and piezoelectric properties†

Madhusudan Dutta,[a] Abhijit Chatterjee,[a] Nilotpal Deka,‡[a] Riteeka Tanwar,‡[a] Vishnu Mishra,[a] Arindam Saha,[b] Pankaj Mandal,*[ac] Ramamoorthy Boomishankar*[ac] and Partha Hazra*[ac]

Received 18th March 2025
Accepted 27th May 2025

DOI: 10.1039/d5sc02107c

rsc.li/chemical-science

Multi-carbazole-based benzonitrile systems are efficient thermally activated delayed fluorescence (TADF) materials for organic light-emitting diodes (OLEDs). However, they suffer from low PLQY due to the large dihedral angle arising from steric crowding. Addressing this challenge, we demonstrate a potent strategy to engineer steric crowding in this work. To achieve our goal, we have designed three luminogens, namely, CzPHCN, tCzPHCN and Cz2CzPHCN based on phenanthrene-9,10-dicarbonitrile (PHCN), as an acceptor core to minimize the steric hindrance between the donor groups. Among the three luminogens, *t*CzPHCN exhibits a maximum PLQY of 86% and the highest RISC rate of 3.5×10^5 s^{-1}, the underlying cause being the least dihedral angle of 45.72° and suppressed intermolecular interaction due to the presence of the bulky *tert*-butyl group. Interestingly, our QM/MM calculations and experimental evidence suggest that the RISC process of both CzPHCN and tCzPHCN takes place *via* a hot exciton channel. Unlocking a new realm of applications, the unique non-centrosymmetric space group ($Cmc2_1$) of CzPHCN offers excellent SHG with a $\chi^{(2)}$ value of 0.21 pm V^{-1} at 1320 nm. In addition to this, the molecule depicts good ferroelectric (P_S = 0.32 μC cm^{-2}), piezoelectric energy harvesting (V_{OC} = 2.8 V) and two-photon absorption properties.

Introduction

Organic luminescent materials exhibiting thermally activated delayed fluorescence (TADF) are making a new frontier in materials science, which can effectively be harnessed for diverse applications, including organic light-emitting diodes (OLEDs), bio-imaging, energy storage, organic photothermal materials, organic lasers, and photocatalysis.[1–7] A distinguishing feature of TADF materials is their ability to harvest non-emissive, electrically generated triplet states and convert them into emissive singlet states *via* reverse intersystem crossing (RISC).[1–3] This RISC mechanism enables TADF emitters to achieve a given internal quantum efficiency (IQE) of 100%, which is four times better than those found in normal fluorescence-based emitters, without the need for heavy-metal incorporation.[1,2] The fundamental design of TADF materials focuses on highly twisted donor–acceptor (D–A) architecture, in which the highest occupied molecular orbital (HOMO) and the lowest unoccupied molecular orbital (LUMO) are spatially separated.[1,8,9] Such structural architecture reduces the singlet–triplet energy gap, ΔE_{ST}, which allows the RISC process to take place.[1,8,9] The orthogonal D–A structure results in nearly degenerate singlet charge-transfer (^{1}CT) and triplet charge-transfer (^{3}CT) states that improve the efficiency of the RISC process.[8,9] However, this twisted configuration also minimizes the overlap between transition orbitals, leading to low oscillator strength and hence, poor photoluminescence quantum yield (PLQY).[10,11] Extensive efforts have been dedicated to develop potential TADF emitters based on multi-carbazole donor and benzonitrile acceptor systems.[1,12–16] In 2012, Uoyama *et al.* reported 4CzIPN, 4CzPN and 4CzTPN as state-of-the-art TADF based on multi-carbazole architecture.[1] However, subsequent studies by Niwa *et al.* revealed that the state-of-the-art TADF emitter 4CzIPN exhibits only 35% PLQY in the neat film state, primarily due to the concentration quenching.[12] Yamanaka *et al.* reported that 4CzTPN shows 15.3% PLQY in concentrated neat film (50 wt% CBP).[13] 4CzPN shows a PLQY of 42%, but its structural analogue, 5CzBN, with an additional carbazole donor, shows

[a]*Department of Chemistry, Indian Institute of Science Education and Research Pune, Dr Homi Bhabha Road, Pune, 411008, India. E-mail: p.hazra@iiserpune.ac.in*
[b]*Catalysis and Inorganic Chemistry Division, CSIR-National Chemical Laboratory, Dr Homi Bhabha Road, Pune 411 008, India*
[c]*Centre for Energy Science, Indian Institute of Science Education and Research Pune, Dr Homi Bhabha Road, Pune, 411008, India*

† Electronic supplementary information (ESI) available: Instrumentation and experimental details, materials and methods, characterization, crystallographic data, computational details. CCDC 2420130, 2420153 and 2420155. For ESI and crystallographic data in CIF or other electronic format see DOI: https://doi.org/10.1039/d5sc02107c

‡ These authors contributed equally to this work.

a significant decrease in PLQY to 21% in neat films.[14,15] Even though promising, these systems still have low PLQY in the solid state and are prone to dimerization that reduces the color purity.[16] The use of multiple carbazole units in these systems induces steric hindrance, forcing adjacent donor groups into nearly orthogonal orientations relative to the acceptor core.[12–15] This geometry promotes stronger inter- and intramolecular interactions, which can further diminish the PLQY. Improvements through systematic molecular engineering are required to enhance PLQY. By judiciously selecting the acceptor core and strategically positioning the donor groups to minimize steric hindrance, the D–A angle can be optimized to enhance transition orbital overlap, thereby improving oscillator strength and PLQY. A moderate ΔE_{ST} with a balanced HOMO–LUMO overlap is a key strategy for enhancing TADF efficiency. This rational design approach may unlock the intrinsic weaknesses of multi-carbazole systems and unleash the full potential of TADF emitters into practical applications.

This study introduces a novel strategy to minimize steric hindrance between donor and acceptor groups, resulting in a reduced D–A angle, improved PLQY, and enhanced TADF efficiency. Previously, Salah *et al.* introduced a new pyrazine-centered acceptor core with multi-carbazole donors, which minimized the intermolecular interaction and achieved a maximum PLQY of 36%.[17] In this work, an extended poly-aromatic system, namely, phenanthrene-9,10-dicarbonitrile (PHCN), is chosen as an acceptor core, and then substituted carbazoles are attached at 3,6- positions of PHCN to minimize steric hindrance. Three carbazole-based emitters – CzPHCN, tCzPHCN and Cz2CzPHCN – were designed using this framework to tune ΔE_{ST}, enhance TADF efficiency and maximize PLQY. All the molecules show excellent PLQY compared to previously reported multi-carbazole systems. Notably, *t*CzPHCN demonstrates the highest PLQY of 86% and has a RISC rate of $\sim 10^6\ s^{-1}$ orders. Additionally, these emitters exhibit broad color tunability, with emissions ranging from green to orange. Furthermore, emitters intrinsically perturb the crystal packing arrangement, which facilitates the manifestation of key phenomena related to nonlinear optical (NLO) properties, such as second harmonic generation (SHG), ferroelectric, piezoelectric and so on.[18,19] Molecular asymmetry in CzPHCN produces a non-centrosymmetric $Cmc2_1$ space group, making it a very good SHG material with a $\chi^{(2)}$ value of 0.21 pm V^{-1} at 1320 nm and laser-induced damage threshold (LIDT) value of 37.82 GW cm^{-2}. Moreover, it shows ferroelectric behaviour with a characteristic rectangular *P–E* hysteresis loop exhibiting a saturation polarization of 0.32 μC cm^{-2} and the piezoelectricity driven energy harvesting behaviour with a maximum peak-to-peak open-circuit voltage (V_{OC}) of 2.8 V and a short circuit current (I_{SC}) of 0.41 μA while attached to a 4.7 MΩ resistor. Moreover, due to the charge transfer nature and large hyperpolarizability,[20] all luminogens exhibit two-photon absorption (TPA) properties (see ESI Section S9†). Based on a comprehensive understanding, this work primarily focuses on molecular engineering to control the molecular level interactions, SHG, ferroelectric and piezoelectric properties.

Results and discussion

Molecular design and synthesis

Considering the impact of the sterically hindered carbazole–benzonitrile core, which exhibits strong interactions,[16] we have designed our luminogens to effectively suppress these interactions. Here, we explore a novel design strategy that extends beyond the conventional use of benzonitrile as an acceptor core.[1,13–15] Specifically, the core structure is modified by fusing two additional benzene rings with the benzonitrile core to form phenanthrene-9,10-dicarbonitrile (PHCN) as the new acceptor core (Scheme 1). This planar, fully conjugated PHCN core is anticipated to exhibit a high emission transition dipole moment, enhancing its photophysical properties.[21] Moreover, the 3 and 6 positions of the PHCN core were strategically selected for donor substitution. This placement ensures a greater spatial separation between donor groups, effectively minimizing intramolecular interactions. This geometry reduces steric hindrance, enabling donor groups to adapt lower dihedral angles relative to the acceptor core. Consequently, considerable HOMO–LUMO overlap is expected to enhance oscillator strength and eventually improve the PLQY. We chose 9H-carbazole (Cz) as the donor moiety, and its donor strength was tuned through the introduction of *tert*-butyl and carbazole groups at the 3 and 6 positions of the parent Cz core. This

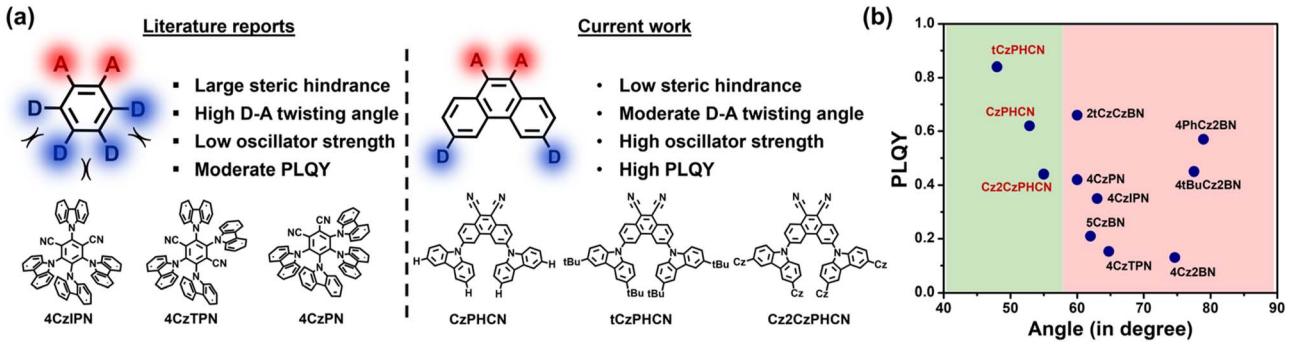

Scheme 1 (a) Molecular designing principle: chemical structure of 4CzIPN, 4CzTPN and 4CzPN from the literature report (left),[1] chemical structure of CzPHCN, *t*CzPHCN and Cz2CzPHCN investigated in this work (right). (b) PLQY *vs.* dihedral angle plot of carbazole-based molecules reported in the literature, and the molecules in this work (see ESI Section S12†).

approach yields two derivatives: 3,6-di-*tert*-butyl-9*H*-carbazole (*t*Cz) and 9′*H*-9,3′ : 6′,9″-tercarbazole (Cz2Cz) (Scheme 1). The specific substitution at the 3,6 positions minimizes steric interactions between the donor and acceptor units, thereby facilitating lower donor–acceptor dihedral angles. As the donor strength increases from Cz to Cz2Cz, the bulkiness and CT characteristics of the molecules change significantly. This variation influences both emission properties and the singlet–triplet energy gap (ΔE_{ST}). A stronger donor reduces the ΔE_{ST}, thereby promoting more efficient RISC and enhancing TADF efficiency. All three molecules, namely, CzPHCN, *t*CzPHCN and Cz2CzPHCN were synthesized by a palladium catalysed Buchwald–Hartwig C–N cross-coupling reaction (Scheme S1†) and purified by the column chromatography technique (40% DCM/hexane) followed by characterization through ^{1}H and ^{13}C NMR, MALDI-TOF and single crystal X-ray diffraction (SCXRD) techniques (see the ESI†).

Theoretical calculations

To understand the electronic nature of our designed donor–acceptor luminogens, density functional theory (DFT) and time-dependent DFT (TD-DFT) calculations were performed. The ground state geometry of all three molecules was optimized by DFT in the B3LYP/6-31g(d,p) level of theory in the gas phase. From the optimized geometry, the dihedral angle between the donor and acceptor (θ_{DA}) is found to be 50.83°, 49.26° and 53.83° for CzPHCN, *t*CzPHCN and Cz2CzPHCN, respectively (Fig. S1†). All the molecules maintain a critical dihedral angle that offers a moderate ΔE_{ST} as well as a high oscillator strength (shaded portion in Fig. 1a–c and S2†). Furthermore, to gain deeper insight into the frontier molecular orbitals (FMOs), TD-DFT calculations were performed (Fig. S3†). The results indicate that the HOMO and LUMO are spatially separated and the HOMO is predominantly localized on the donor moieties, while the LUMO is primarily concentrated on the acceptor segment. The HOMO–LUMO overlap was quantitatively assessed using Multiwfn software.[22] The analysis revealed that the overlap for CzPHCN and tCzPHCN is nearly three times greater than that of Cz2CzPHCN (Table S1†).

Single crystal X-ray diffraction analysis

The single crystal X-ray crystallographic data show that CzPHCN crystallizes in the non-centrosymmetric $Cmc2_1$ space group and *t*CzPHCN and Cz2CzPHCN crystallize in the centrosymmetric $P2_1/c$ and $P\bar{1}$ space group, respectively (Tables S2–S4 and Fig. S6†). From SCXRD data, it is evident that the donor–acceptor dihedral angle ranges from 45.72° to 57.13° (Fig. 2a–c), this is in close agreement with our theoretical calculations, validating that the chosen level of theory appropriately corroborates the experimental outcomes (Fig. S1†). For the reported carbazole–benzonitrile core, due to the close proximity of the multiple carbazole units, they face strong steric hindrance and orient themselves in a near orthogonal geometry with respect to benzonitrile to minimize the steric effect, resulting in strong π–π interaction. 4CzIPN shows intermolecular π–π interaction with the carbazole moiety with a distance of 3.379 Å (Fig. S7†).[16,17] But 4CzTPN exhibits almost fully overlapped carbazole moieties at a distance of 3.488 Å and 3.279 Å

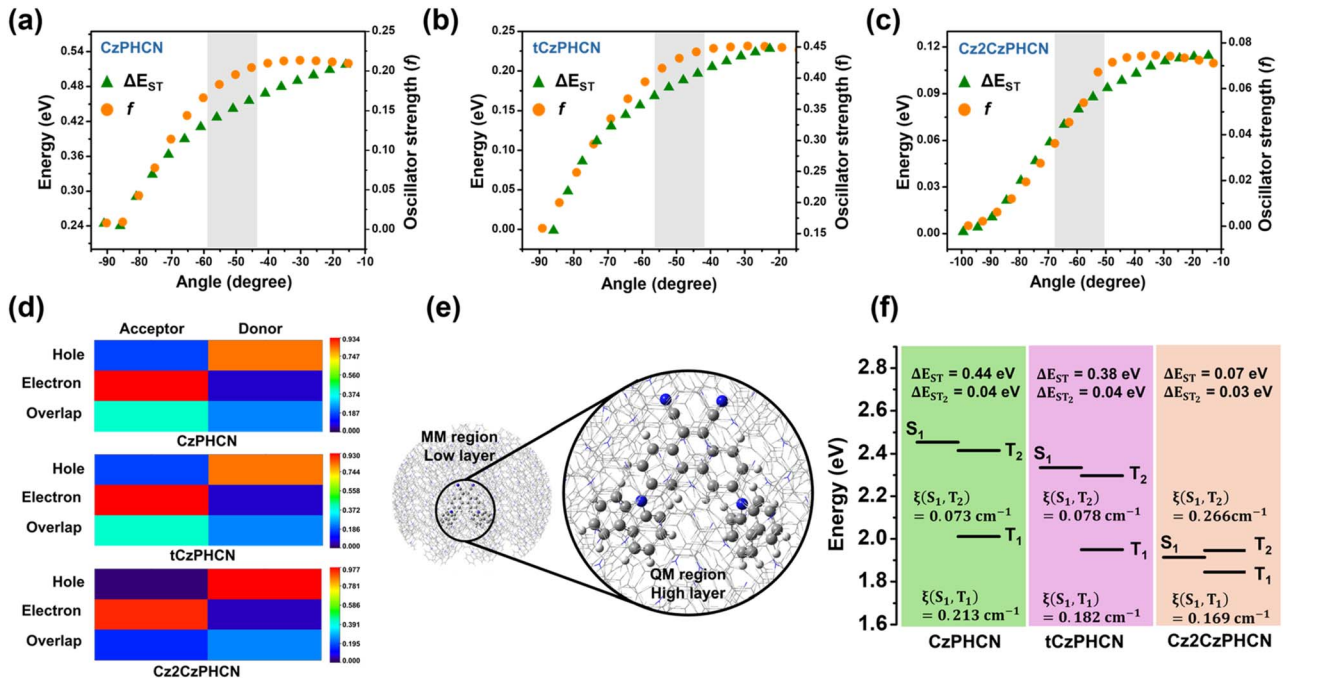

Fig. 1 Plot of ΔE_{ST} and oscillator strength *vs.* dihedral angle (θ_{DA}) of (a) CzPHCN, (b) *t*CzPHCN and (c) Cz2CzPHCN. (d) The heat maps of the distribution of electron–hole in the donor and acceptor moiety in the S_1 state. (e) High layer (QM region) and low layer (MM region) from the crystal structure for QM/MM calculation. (f) Single point energies and spin–orbit coupling (SOC) from TD-DFT calculation based on QM/MM calculation.

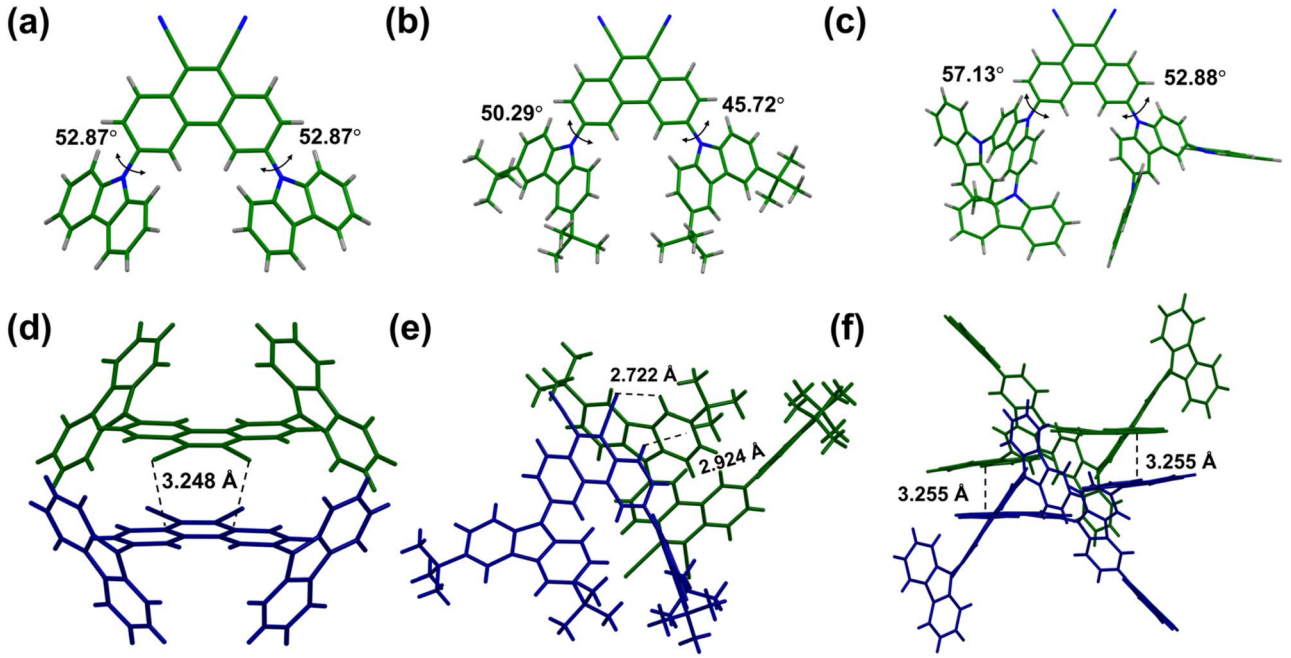

Fig. 2 Crystal structure of (a) CzPHCN, (b) *t*CzPHCN and (c) Cz2CzPHCN with the donor–acceptor dihedral angle (θ_{DA}). Crystal packing interaction of (d) CzPHCN, (e) *t*CzPHCN and (f) Cz2CzPHCN.

(Fig. S7†). In contrast, for our PHCN core, the two carbazole units are placed far apart, resulting in negligible interaction (Fig. S8–S10†). This arrangement allows for a lower dihedral angle with the PHCN core, facilitating better overlap between the HOMO and LUMO, which leads to a higher oscillator strength compared to the reported carbazole–benzonitrile core. SCXRD analysis shows that CzPHCN and *t*CzPHCN do not exhibit any π–π stacking interaction, whereas Cz2CzPHCN exhibits intermolecular π–π interaction between extended carbazole moieties and acceptor core at a distance of 3.255 Å (Fig. 2d–f and S8, S10†). Interestingly, the introduction of two bulky *tert*-butyl groups in *t*CzPHCN keeps the adjacent molecules far apart, resulting in the lowest intermolecular interaction among the three investigated molecules (Fig. S8–S10†).

Photophysical properties

In a non-polar solvent, like toluene, all three compounds display two absorption bands: one high-energy structured band around 320–340 nm and another low-energy broad band around 405–450 nm (Fig. 3a). The high-energy band is attributed to π–π* transition and the low-energy broad band is attributed to intramolecular charge-transfer transition from the donor to the acceptor moieties. All three luminogens display a broad, structureless emission band in toluene, with peak maximum at approximately 485 nm, 510 nm, and 565 nm for CzPHCN, *t*CzPHCN, and Cz2CzPHCN, respectively (Fig. 3a). This trend indicates a progressive stabilization of the S_1 state from CzPHCN to Cz2CzPHCN. Moreover, such stabilization stems from an increasing donating strength on going from CzPHCN to Cz2CzPHCN, which is consistent with our theoretical calculations – CzPHCN exhibits the highest HOMO–LUMO overlap and Cz2CzPHCN shows the least HOMO–LUMO overlap (Table S1†). The nature of the molecules is further supported by polarity-dependent studies, which show a redshift in emission with increasing polarity (Fig. S11†). CzPHCN, *t*CzPHCN, and Cz2CzPHCN exhibit redshifts of 74 nm, 87 nm, and 110 nm, respectively. This indicates that the S_1 state of Cz2CzPHCN has the strongest CT character, while CzPHCN shows the weakest CT character. This finding aligns with our natural transition orbital (NTO) analysis (Fig. S4†), which shows that the electron and hole wavefunctions of the S_1 state are spatially separated, clearly demonstrating the CT nature of the emissive state. For quantitative analysis, the electron–hole orbital overlaps between the donor and acceptor cores were evaluated using heat maps (Fig. 1d). These results indicate that Cz2CzPHCN exhibits the highest CT character, attributed to the enhanced donor strength of Cz2Cz. It is noteworthy that the time-resolved photoluminescence (TRPL) decay kinetics reveal only a nanosecond component in the solution state (Fig. S12†) and is devoid of any longer component in the μs timescale. Moreover, from the solution to the aggregated state, all emitters show aggregation-induced emission (AIE) properties (see ESI Section S8†).

For practical device fabrication, it is essential to develop a comprehensive understanding of the excited-state dynamics and photophysical properties of emitters in the solid state. To evaluate the photophysical properties of the emitters in the solid state, spin-coated neat films were prepared. These films display emission behavior consistent with the trends observed in their solution-state counterparts, exhibiting distinct emission maxima at 545 nm, 575 nm, and 605 nm for CzPHCN, *t*CzPHCN, and Cz2CzPHCN, respectively (Fig. 3d–f).

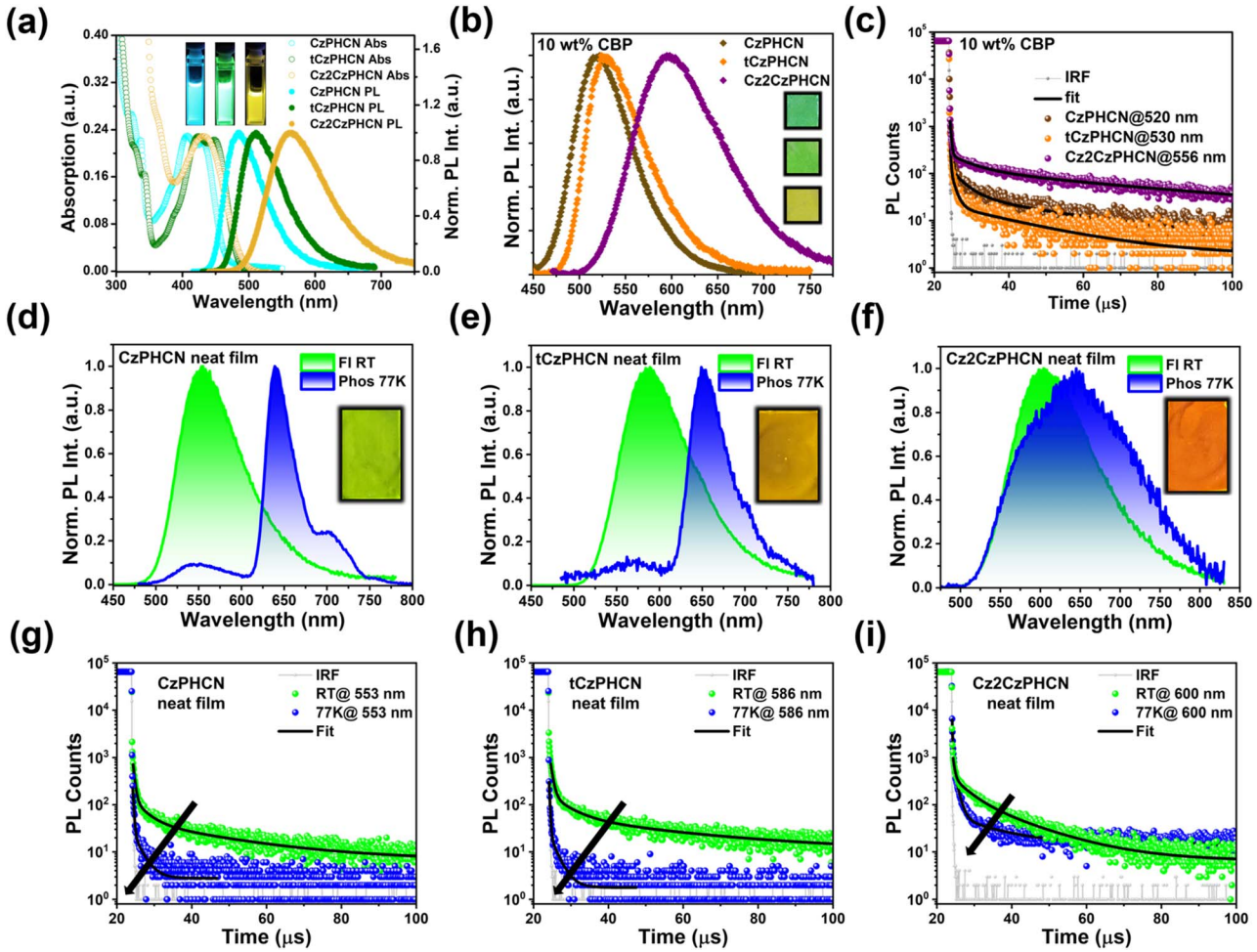

Fig. 3 (a) Absorption and emission spectra of emitters in 10 μM toluene solution. (b) Emission spectra of 10 wt% CBP doped emitters. (c) Delayed lifetime of 10 wt% CBP doped emitters. Fluorescence spectra (green) and phosphorescence spectra (blue) of (d) CzPHCN, (e) *t*CzPHCN and (f) Cz2CzPHCN in neat film. Delayed lifetime of (g) CzPHCN, (h) *t*CzPHCN and (i) Cz2CzPHCN at RT (green) and 77 K (blue). All the lifetimes are collected on fluorescence peak maxima. For PL spectra of CzPHCN and *t*CzPHCN, excitation was 400 nm and for Cz2CzPHCN, 430 nm excitation was used. 355 nm spectraLED was used as the excitation source to measure delayed lifetime.

Interestingly, unlike in the solution state, along with a short prompt fluorescence decay in ns timescale (Fig. S13†), the time-resolved PL decay dynamics at room temperature exhibit delayed lifetime of 2.4 μs, 3.2 μs and 4.3 μs, for CzPHCN, *t*CzPHCN, and Cz2CzPHCN, respectively (Fig. 3g–i). The presence of this delayed lifetime in the solid state suggests that a spin-flip process is involved in the emission mechanism. To investigate the origin of this process, temperature-dependent transient PL decay measurements were performed. A notable reduction in the delayed emission lifetime was observed as the temperature decreased from room temperature to 77 K. This behavior indicates the occurrence of a thermally activated delayed fluorescence (TADF) process. At cryogenic temperatures, the exciton transfer from the triplet to the singlet state is suppressed due to insufficient thermal energy, thereby inhibiting the TADF mechanism and reducing its lifetime. Furthermore, gated emission spectra were collected at a 5 ms delay at 77 K, revealing that the S_1 emission almost disappears at lower temperatures and a new red-shifted emission peak emerges at 635 nm, 660 nm, and 644 nm for CzPHCN, *t*CzPHCN, and Cz2CzPHCN, respectively (Fig. 3d–f). These peaks, with lifetimes of 16.1 ms, 14.6 ms, and 86.6 ms (Fig. S14†), are attributed to phosphorescence from the T_1 state. From the onset of fluorescence and phosphorescence spectra at room temperature and 77 K, ΔE_{ST} values were calculated as 0.468 eV, 0.358 eV, and 0.014 eV for CzPHCN, *t*CzPHCN, and Cz2CzPHCN, respectively (Fig. S15†). The theoretically evaluated ΔE_{ST} values are 0.44 eV, 0.38 eV and 0.014 eV for CzPHCN, *t*CzPHCN, and Cz2CzPHCN, respectively (Fig. 1f), showing close agreement with the experimentally determined ΔE_{ST} values. From the ΔE_{ST} values, it is clear that for Cz2CzPHCN, RISC can occur from the T_1 to the S_1 state as the ΔE_{ST} falls within the range of thermal energy (<0.3 eV) (Fig. S5a†). But for the other two cases, the ΔE_{ST} is large compared to thermal energy, although they also exhibit TADF property. To gain insight into this mechanism, TD-DFT calculations were performed using the two-layer QM/MM model with optimized crystal geometry as input (Fig. 1e).[23] From the energy alignment of the electronic states, it was observed that the T_2

Table 1 All photophysical data of the three luminogens in the neat film state. All the quantum yields are measured using an integrating sphere under ambient conditions. ϕ_{PF} and ϕ_{DF} are fractional prompt fluorescence quantum yield and delayed fluorescence quantum yield

Luminogens in neat film	PL (nm)	ϕ^a	ϕ_{PF}	ϕ_{DF}	τ_{PF} (ns)	τ_{DF} (μs)	k_r (10^7 s^{-1}) ($S_1 \rightarrow S_0$)^b	k_{ISC} (10^7 s^{-1}) ($S_1 \rightarrow T_1$)^c	k_{RISC} (10^5 s^{-1}) ($T_1 \rightarrow S_1$)^d	ΔE_{ST} (eV)
CzPHCN	545	0.62	0.53	0.09	5.24	2.4	10.2	8.87	1.39	0.468
*t*CzPHCN	575	0.86	0.58	0.28	8.04	3.2	7.22	5.22	3.54	0.358
Cz2CzPHCN	605	0.44	0.29	0.15	5.88	4.3	4.92	12.1	1.71	0.014

^{a} ϕ is the total PLQY measured under ambient conditions. ^{b} k_r ($S_1 \rightarrow S_0$) = ϕ_{PF}/τ_{PF}. ^{c} k_{ISC} ($S_1 \rightarrow T_1$) = $(1 - \phi_{PF})/\tau_{PF}$. ^{d} k_{RISC} ($T_1 \rightarrow S_1$) = $\phi_{DF}/(k_{ISC}\phi_{PF}\tau_{DF}\tau_{PF})$.

state is in close proximity to the S_1 state, both for CzPHCN and *t*CzPHCN, with an energy gap of only 0.04 eV (Fig. 1f). This energy alignment facilitates the exciton up-conversion to the S_1 state *via* a hot exciton channel, *i.e.*, from the T_2 state, instead of the direct T_1 state (Fig. S5b†). The process of RISC through a hot exciton channel is relatively rare among organic emitters due to its complicated design and challenging electronic requirements.[24,25] This hot RISC observed in CzPHCN and *t*CzPHCN enables us to achieve a shorter delayed lifetime and high radiative rate compared to Cz2CzPHCN (Table 1). The absolute PLQY measurement in neat films of our molecules shows very high PLQY as compared to previously reported multi-carbazole systems. Unlike the multi-carbazole system, substituting at only 3 and 6 positions of the PHCN core, the donor groups experience less steric crowding. This results in a moderately low D–A angle and greater HOMO–LUMO overlap, leading to a higher oscillator strength in these molecules. Among the three molecules, *t*CzPHCN demonstrates an outstanding PLQY of 86% in the neat film state, while CzPHCN and Cz2CzPHCN exhibit very good PLQY of 62% and 44%, respectively (Fig. S16–S18†). To better understand the variation in PLQY, the crystal structures were critically examined. In Cz2CzPHCN, face-to-face π–π intermolecular interactions between carbazole moieties are observed (Fig. 2f and S8†), which contribute to a reduced PLQY of 44%. However, the incorporation of bulky *tert*-butyl groups in tCzPHCN hinders the close packing of adjacent molecules, effectively suppressing intermolecular interactions (Fig. 2e and S8†). This structural modification enables *t*CzPHCN to achieve its exceptionally high PLQY. In contrast, 4CzIPN and 4CzTPN exhibit a poor PLQY of 35% and 15.3%, respectively, due to pronounced face-to-face intermolecular π–π interactions between carbazole units.[12,13] The RISC rates were calculated from the fractional quantum yield of prompt fluorescence (ϕ_{PF}) and delayed fluorescence (ϕ_{DF}) which are estimated by calculating the area under the curve of PL spectra taken under ambient and vacuum conditions (Fig. S19†).[26] Among all the three emitters, *t*CzPHCN shows the highest RISC (3.54×10^5 s^{-1}) (Table 1) due to the combined effect of high ϕ_{DF} and a very low S_1–T_2 energy gap.

Studying the photophysical properties of emitter-doped host matrix films is essential for assessing their suitability in OLED devices and for minimizing concentration quenching effects. In this context, 4,4′-bis(*N*-carbazolyl)-1,1′-biphenyl (CBP) was selected as a host material due to its high triplet energy (2.58 eV) that can efficiently suppress back energy transfer from the guest to the host molecule.[27] Spin-coated 10 wt% emitter doped films of CzPHCN, *t*CzPHCN and Cz2CzPHCN exhibit emission peaks at 520 nm, 530 nm and 556 nm, respectively (Fig. 3b). Transient PL decays were collected at peak maxima, exhibiting delayed lifetime of 1.4 μs, 0.91 μs and 5.1 μs, respectively (Fig. 3c), for CzPHCN, *t*CzPHCN and Cz2CzPHCN along with a short nanosecond component (Fig. S20†), suggesting the presence of TADF property in all three molecules even in the doped film state. The absolute PLQYs of CzPHCN, *t*CzPHCN and Cz2CzPHCN are 78%, 94% and 70%, respectively (Fig. S21–S23†). For Cz2CzPHCN, the PLQY almost doubled compared to the neat film. This enhancement is attributed to the dilution effect, where the increased distance between neighboring molecules minimizes intermolecular π–π interactions between carbazole moieties, leading to a higher PLQY in the doped-film state compared to the neat film. The RISC rates in the doped film follow a similar trend as that of the neat film state, but for *t*CzPHCN, the RISC rate (11.6×10^5 s^{-1}) increases three times as compared to neat films due to its fast delayed lifetime in the doped film (Table S5 and Fig. S24†). Considering all these results, *t*CzPHCN exhibits maximum TADF efficiency in both neat and doped films with a very high RISC rate of $\sim 10^6$ s^{-1}. In contrast, the reported 4CzIPN and 4CzTPN exhibit a similar order of RISC rates; however, they show significantly reduced PLQY due to intermolecular interactions.[12,13] These interactions facilitate electron exchange between neighbouring molecules, followed by non-radiative decay from the triplet state to the ground state. Moreover, examining all the structural motifs, it is evident that the two ortho positions of the acceptor core with respect to the attached carbazole are essential to make the system more planar. Unlike these systems, ortho positions of multi-carbazole-based 4CzIPN and 4CzTPN are blocked by either another carbazole or nitrile group,[17] making the system more twisted to avoid steric crowding. These twisted conformations allow stacking interaction with neighboring molecules which are absent in these newly designed emitters reported in this work. Thus, engineering the steric environment of multi-carbazole emitters allows us to achieve the low dihedral angle between the donor and acceptor, which eventually boosts the PLQY and TADF efficiency of these emitters.

Second harmonic generation

In recent years, nonlinear optics has become the foundation for numerous advanced technologies, including light frequency

upconversion, lasing, ultraviolet light generation, bio-imaging, photodetection, and optical communication systems.[28,29] Nonlinear optics explores the interactions between materials and intense laser sources, with second harmonic generation (SHG) and third harmonic generation (THG) being key processes. Notably, organic luminescent materials exhibiting TADF have recently demonstrated significant potential in nonlinear optical (NLO) applications.[18] In this study, we examined the nonlinear optical response of our material, specifically focusing on its SHG properties. A fundamental prerequisite for any material to exhibit second-order nonlinear processes is the absence of inversion symmetry. Among the three synthesized molecules, CzPHCN satisfies this criterion by exhibiting a non-centrosymmetric structure and crystallizing in the orthorhombic $Cmc2_1$ space group, making it a promising candidate for SHG response.

We investigated the NLO properties of CzPHCN through an in-depth analysis of its SHG behavior, focusing on SHG efficiency, optical stability, and structural anisotropy. Ultrafast pulses with a pulse width of approximately 50 fs, generated by an optical parametric amplifier (OPA) powered by a regenerative amplifier, were employed as the excitation source for the SHG experiments. Detailed information regarding the experimental setup and methodology is provided in ESI Section S10 (Fig. S33†).

The SHG response of the non-centrosymmetric CzPHCN was measured at various excitation wavelengths ranging from 1200 to 1440 nm while maintaining a constant excitation power of 1 mW (Fig. 4a). The measurements revealed significant variations in both the nature and intensity of the SHG spectra. A pronounced enhancement of the SHG response was observed near 660 nm, corresponding to an excitation wavelength of 1320 nm. It is intriguing to note that the peak of the SHG response (Fig. 4b) nearly coincides with the phosphorescence peak, indicating a resonance enhancement of SHG due to the T_1 state of the molecule. Furthermore, the second-order nonlinear susceptibility ($\chi^{(2)}$) of CzPHCN was determined using Maxwell's relative intensity equation.[30] Potassium dihydrogen phosphate (KDP), a widely used reference material for SHG studies, was employed as the benchmark to evaluate the second-order nonlinear susceptibility ($\chi^{(2)}$) of CzPHCN. Detailed calculations and methodology are provided in the ESI (Fig. S34†). At 1064 nm, KDP has a reported $\chi^{(2)}$ value of 0.37 pm V^{-1}.[30,31] The $\chi^{(2)}$ value of CzPHCN at 1064 nm was determined to be 0.128 pm V^{-1}. Additionally, by comparing the SHG intensity of CzPHCN at the reference wavelength with its intensity at the wavelength corresponding to the maximum SHG response, the $\chi^{(2)}$ value of CzPHCN at 1320 nm was determined to be 0.21 pm V^{-1}. This analysis highlights the strong nonlinear optical response of CzPHCN across different wavelengths, further underscoring its potential in NLO applications.

The laser-induced damage threshold (LIDT) is a key parameter that quantifies a material's optical stability, representing the maximum energy density the material can endure without damage under high-power excitation.[32] The LIDT for SHG corresponds to the power at which the SHG response ceases to follow a quadratic relationship with the excitation power. To assess the LIDT of our material, we recorded its power-dependent SHG response at the excitation wavelength of 1320 nm, corresponding to the maximum SHG response. The SHG response exhibited a quadratic dependence on the excitation power (Fig. 4c), consistent with a second-order nonlinear process, up to 9.5 mW. Beyond this power level, deviations from the quadratic behavior were observed, likely due to saturation effects caused by local heating.[33] The LIDT value was determined to be approximately 37.82 GW cm^{-2} (details in ESI Section 10†). The LIDT value of our material is comparable to that of benchmark lead halide perovskites,[33–35] indicating its potential suitability for real-world NLO applications.

Next, we have investigated the structural anisotropy by analyzing the variation in SHG intensity with the changes in the polarization angle of the excitation source. Measurements were conducted under resonance conditions, with the maximum SHG intensity recorded at an excitation power of 1 mW. The SHG intensity exhibits a two-lobed distribution, with the maximum intensity occurring when the polarization axis is perpendicular to the crystal's optical axis (Fig. 4d).[34] Conversely, the minimum intensity is observed when the polarization axis is parallel to the crystal axis. These results highlight the critical role of crystal symmetry in determining the SHG emission pattern, emphasizing the sensitivity of SHG to structural anisotropy. The polarization ratio of the CzPHCN crystal was determined to be 46% (see ESI Section S10†).

Though SHG is frequently observed in non-centrosymmetric systems, there are reports of SHG even from some centrosymmetric crystals.[36–38] Hence, we have investigated the SHG properties of the other centrosymmetric compounds as well. We

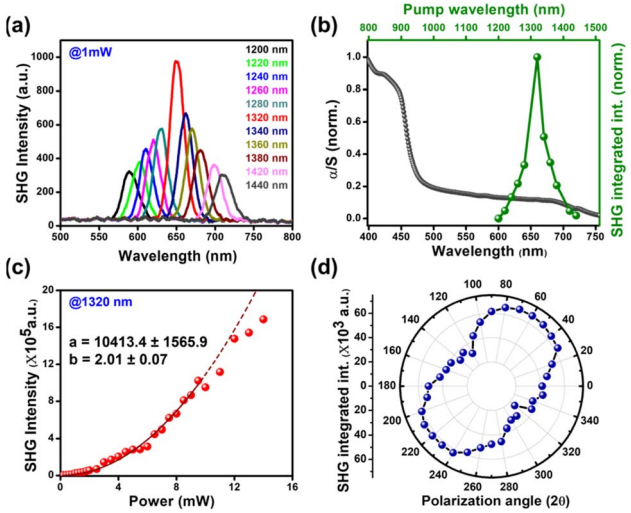

Fig. 4 Nonlinear SHG response of the CzPHCN crystal. (a) Excitation wavelength-dependent SHG response measured across a range of pump excitation wavelengths from 1200 to 1440 nm at a constant power of 1 mW. (b) SHG integrated intensity as a function of both SHG wavelength and excitation wavelength. (c) Excitation power dependent SHG response at a fixed excitation wavelength of 1320 nm. The dashed line is the quadratic fit to the experimental data. (d) Polarization-dependent SHG intensity of the crystal as a function of polarization angle at 1320 nm with a constant excitation power.

have not observed any SHG signal for both tCzPHCN and Cz2CzPHCN. Instead, a strong photoluminescence (PL) independent of excitation wavelength was detected (Fig. S35a and b†). Additionally, a weak THG response was observed. In contrast to PL, the THG response varied with excitation wavelength (Fig. S35a and b†), and both PL and THG intensities increased with rising excitation power (Fig. S35c and d†). It is possible that a stronger and broad PL suppressed the weak SHG from the centrosymmetric compound. TADF materials with SHG properties are rare in the literature, however, there are some theoretical studies on NLO properties of TADF emitters.[39,40] Very recently, Chatterjee *et al.* reported emitters with both TADF and SHG properties.[18] It is observed that the performance of the SHG output of CzPHCN is comparable with that of reported DPAOCN (Table S6†).[18] But LIDT values indicate that CzPHCN is much more optically stable than DPAOCN.

Application

Converted LED

The high PLQY of the emitters in both doped and neat film underscores their potential for application in OLED devices. In this context, polymethyl methacrylate (PMMA) was chosen as a host matrix due to its high triplet energy states, which not only suppress back energy transfer from the emitter to the host but also provide a rigid environment to reduce nonradiative pathways.[41] c-LEDs were fabricated by using 10 wt% emitter-doped PMMA on InGaN chips. Under a 3 V bias, CzPHCN and *t*CzPHCN emit a greenish-yellow color with CIE coordinates of (0.42, 0.54) and (0.45, 0.51), respectively, while Cz2CzPHCN exhibits yellow emission with CIE coordinates of (0.46, 0.51) (Fig. 5). This experiment highlights the potential use of these three emitters in the development of OLEDs.

Ferroelectricity and piezoelectricity

Organic small molecule-based ferroelectric materials are recently emerging as promising candidates because of their unique advantages of non-toxicity, lightweight, structural tunability, and low-temperature processing.[19,42] Despite various design strategies being employed for ferroelectricity, carbazole-based single-component molecular ferroelectrics remain largely underexplored. Carbazole-engineered CzPHCN, owing to its non-centrosymmetric structure and crystallization in the polar orthorhombic $Cmc2_1$ space group, is also being investigated for its ferroelectric and piezoelectric energy harvesting properties. CzPHCN exhibits the C_{2v} point group symmetry, which belongs to one of the 10 polar point groups compatible with ferroelectric properties. Polarization *vs.* electric field (*P*–*E*) hysteresis loop measurements (Fig. 6a) were conducted on CzPHCN drop cast thin film on ITO-coated glass using a Sawyer–Tower circuit setup (Fig. 6b) at room temperature to investigate its ferroelectric response. A typical rectangular-shaped *P*–*E* loop was observed at 298 K with the saturation polarization (*P*s) value of 0.32 μC cm^{-2} comparable to those reported for several ferroelectric materials (Table S7†).

Subsequently, a home-built impact setup coupled with an oscilloscope was utilized to explore the performance of CzPHCN as a piezoelectric nanogenerator (energy harvester). Under consistent conditions, with a fixed force of 21 N and a frequency of 10 Hz, the nanogenerator made by sandwiching the neat crystallites of CzPHCN, revealed a peak-to-peak voltage of 2.8 V in an open circuit configuration (Fig. 6c and Table S8†). When connected to a 4.7 MΩ resistor, the calculated peak-to-peak short circuit current was measured to be 0.41 μA. Polarity reversal measurements were conducted to assess the reliability of the obtained voltage by altering the connections to the oscilloscope. These experiments yielded the sustained peak-to-peak voltage, accompanied by the generation of reverse signals with opposing magnitudes, confirming the piezoelectric origin of the obtained voltages (Fig. 6d).

The ferroelectric and piezoelectric properties of the state-of-the-art TADF emitters are unexplored. Combining TADF with ferroelectric and piezoelectric properties is a burgeoning research direction, which might lead to innovative optoelectronic, sensing, or energy-harvesting devices. To the best of our knowledge, for the first time, we are reporting ferroelectric, piezoelectric and TADF properties in an organic molecule. Notably, ferroelectricity and piezoelectricity demand a non-

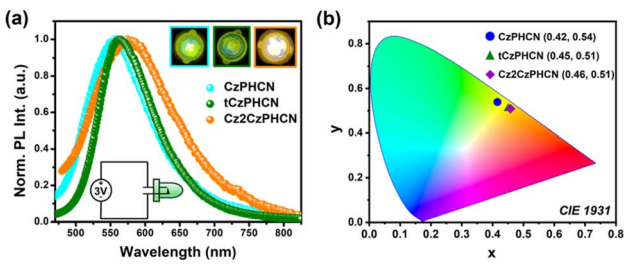

Fig. 5 (a) Emission spectrum of all three emitter-fabricated c-LEDs. (b) Chromaticity plots (CIE 1931) of all emitters.

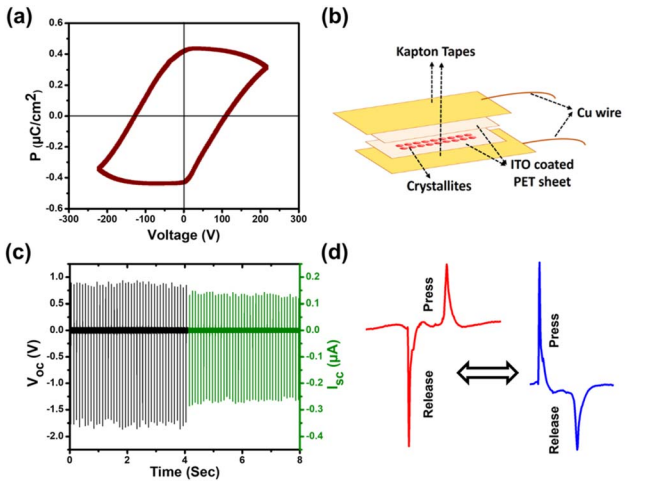

Fig. 6 (a) *P*–*E* hysteresis loop for CzPHCN. (b) Schematic showing the fabrication of a piezoelectric nanogenerator device. (c) Open circuit peak-to-peak voltage (V_{PP}) and calculated short-circuit current (I_{PP}) of as-made piezo device (the shifted time axis provided here is a guide to the eye). (d) Peak-to-peak voltage profiles for a single cycle of signals in the forward and reverse polarity connections.

centrosymmetric crystal space group. The state-of-the-art TADF emitters, such as 4CzIPN and 4CzTPN, have a centrosymmetric space group (4CzIPN CCDC No.: 1873416, 4CzTPN CCDC No.: 1873425)[16] and therefore, those molecules do exhibit ferroelectric and piezoelectric properties. Thus, it is a challenging job to design a non-centrosymmetric crystal that also displays TADF property. Probably, due to these reasons, this area of research remains unexplored. We have comapred the ferroelectric (Table S7†) and piezoelectric (Table S8†) properties of our compound with some reported non-TADF small organic molecules in Section S11†. The values indicate reasonable ferroelectric and piezoelectric performance of our compound.

Conclusions

In this work, we strategically modulated steric hindrance to enhance PLQY and accelerate RISC, thereby achieving an efficient TADF emitter. To achieve our objective, we have synthesized a series of phenanthrene–carbazole-based TADF systems having a moderately lower dihedral angle compared to well-known carbazole–benzonitrile systems having low PLQY due to the large dihedral angle and strong intermolecular interactions. Extensive theoretical and photophysical studies were conducted to establish a clear structure–property relationship, highlighting the superior performance of *t*CzPHCN. This emitter exhibits a unique crystal packing with minimal interaction, near unity PLQY and a rapid RISC rate ($\sim 10^5$ s^{-1}), demonstrating its potential as a highly efficient TADF emitter. To the best of our knowledge, this is the first ever report of a carbazole-phenanthrene-based TADF emitter demonstrating a remarkably high PLQY with a low dihedral angle and minimum intermolecular interactions. Interestingly, our QM/MM calculations and experimental evidence suggest that the RISC process of both CzPHCN and *t*CzPHCN takes place *via* a higher triplet state, *i.e.*, through a hot exciton channel. Moreover, non-centrosymmetric CzPHCN exhibits SHG property with a high $\chi^{(2)}$ value of 0.21 pm V^{-1} at 1320 nm with an LIDT value of 37.82 GW cm^{-2}. The ferroelectric measurements on it gave a well-saturated rectangular loop with a *P* value of 0.32 μC cm^{-2}, while the piezoelectric energy harvesting studies yielded a maximum V_{OC} of 2.8 V, evidencing the multifunctional nature of this material. Finally, a converted LED (cLED) was fabricated using our newly designed emitters to explore its applicability in optoelectronic devices.

Data availability

All the supporting data associated with this work are available in the ESI.†

Author contributions

M. D. and P. H. conceived the idea of the project. M. D. is the principal contributor for the execution of the whole project. M. D. and P. H. wrote the manuscript. A. C. helped in the two-photon absorption experiment and manuscript corrections. N. D. and R. T. contributed equally. Under the supervision of R. B., N. D. performed piezoelectric and ferroelectric measurements. Under the supervision of P. M., R. T. performed the SHG experiment. V. M. solved the crystal structures. A. S. provided the photochemical set-up for the photochemical cyclisation reaction. All the authors helped to revise the manuscript. P. H. supervised the whole project and gave valuable insights.

Conflicts of interest

There are no conflicts to declare.

Acknowledgements

P. H. thanks the Ministry of Education, Government of India, (Grant MoE-STARS/STARS-2/2023-0313) for the financial support. P. M. thanks DST Nano Mission for financial support through Grant DST/NM/TUE/QM-10/2019 (C)/4. P. H. acknowledges PARAM Brahma Facility under the National Supercomputing Mission, Government of India. P. H. thanks Mr Vijay Vittal from the Microscopic facility, IISER Pune. P. H. thanks Dr Santhosh Babu Sukumaran, CSIR-NCL Pune for instrument support. P. H. also thanks Mr Animesh Ghosh from Dr Angshuman Nag lab, IISER Pune for PL measurement in vacuum. R. T. and N. D. acknowledge UGC, India and PMRF, India for fellowship, respectively.

References

1 H. Uoyama, K. Goushi, K. Shizu, H. Nomura and C. Adachi, *Nature*, 2012, **492**, 234–238.
2 S. Qi, S. Kim, V. N. Nguyen, Y. Kim, G. Niu, G. Kim, S. J. Kim, S. Park and J. Yoon, *ACS Appl. Mater. Interfaces*, 2020, **12**, 51293–51301.
3 F. Y. Meng, I. H. Chen, J. Y. Shen, K. H. Chang, T. C. Chou, Y. A. Chen, Y. T. Chen, C. L. Chen and P. T. Chou, *Nat. Commun.*, 2022, **13**, 1–10.
4 J. R. Caine, H. Choi, R. Hojo and Z. M. Hudson, *Chem.–Eur. J.*, 2024, **30**, e202302861.
5 S. Li, J. Chen, Y. Wei, J. De, H. Geng, Q. Liao, R. Chen and H. Fu, *Angew. Chem., Int. Ed.*, 2022, **61**, e202209211.
6 M. A. Bryden and E. Zysman-Colman, *Chem. Soc. Rev.*, 2021, **50**, 7587–7680.
7 M. Hosseinnezhad, S. Nasiri, V. Nutalapati, K. Gharanjig and A. M. Arabi, *Prog. Color, Color. Coat.*, 2024, **17**, 417–433.
8 K. Nasu, T. Nakagawa, H. Nomura, C. J. Lin, C. H. Cheng, M. R. Tseng, T. Yasuda and C. Adachi, *Chem. Commun.*, 2013, **49**, 10385–10387.
9 T. Nakagawa, S. Y. Ku, K. T. Wong and C. Adachi, *Chem. Commun.*, 2012, **48**, 9580–9582.
10 W. Huang, M. Einzinger, T. Zhu, H. S. Chae, S. Jeon, S. G. Ihn, M. Sim, S. Kim, M. Su, G. Teverovskiy, T. Wu, T. Van Voorhis, T. M. Swager, M. A. Baldo and S. L. Buchwald, *Chem. Mater.*, 2018, **30**, 1462–1466.
11 W. Huang, M. Einzinger, A. Maurano, T. Zhu, J. Tiepelt, C. Yu, H. Sik Chae, T. Van Voorhis, M. A. Baldo, S. L. Buchwald, W. Huang, T. Zhu, T. Van Voorhis, S. L. Buchwald, C. Yu, M. Einzinger, J. Tiepelt, M. A. Baldo,

A. Maurano and H. S. Chae, *Adv. Opt. Mater.*, 2019, **7**, 1900476.
12 A. Niwa, T. Kobayashi, T. Nagase, K. Goushi, C. Adachi and H. Naito, *Appl. Phys. Lett.*, 2014, **104**, 213303.
13 T. Yamanaka, H. Nakanotani and C. Adachi, *Sci. Adv.*, 2022, **8**, 9188.
14 Q. Chen, Y. Liu, X. Guo, J. Peng, S. Garakyaraghi, C. M. Papa, F. N. Castellano, D. Zhao and Y. Ma, *J. Phys. Chem. A*, 2018, **122**, 6673–6682.
15 X. Ban, A. Zhu, T. Zhang, Z. Tong, W. Jiang and Y. Sun, *ACS Appl. Mater. Interfaces*, 2017, **9**, 21900–21908.
16 M. K. Etherington, N. A. Kukhta, H. F. Higginbotham, A. Danos, A. N. Bismillah, D. R. Graves, P. R. McGonigal, N. Haase, A. Morherr, A. S. Batsanov, C. Pflumm, V. Bhalla, M. R. Bryce and A. P. Monkman, *J. Phys. Chem. C*, 2019, **123**, 11109–11117.
17 L. Salah, M. K. Etherington, A. Shuaib, A. Danos, A. A. Nazeer, B. Ghazal, A. Prlj, A. T. Turley, A. Mallick, P. R. McGonigal, B. F. E. Curchod, A. P. Monkman and S. Makhseed, *J. Mater. Chem. C*, 2021, **9**, 189–198.
18 A. Chatterjee, J. Chatterjee, S. Sappati, R. Tanwar, M. D. Ambhore, H. Arfin, R. M. Umesh, M. Lahiri, P. Mandal and P. Hazra, *Chem. Sci.*, 2023, **14**, 13832–13841.
19 S. Sahoo, S. Mukherjee, V. B. Sharma, W. I. Hernández, A. C. Garcia-Castro, J. K. Zaręba, D. Kabra, G. Vaitheeswaran and R. Boomishankar, *Angew. Chem., Int. Ed.*, 2024, **63**, e202400366.
20 P. A. Shaw, E. Forsyth, F. Haseeb, S. Yang, M. Bradley and M. Klausen, *Front. Chem.*, 2022, **10**, 921354.
21 N. J. Turro, V. Ramamurthy and J. C. Scaiano, *Modern Molecular Photochemistry of Organic Molecules*, University Science Books, CA, 2010.
22 T. Lu and F. Chen, *J. Comput. Chem.*, 2012, **33**, 580–592.
23 H. Li, X. Wang, K. Yuan, L. Lv and Z. Li, *Phys. Chem. Chem. Phys.*, 2021, **23**, 20218–20229.
24 J. M. Jacob and M. K. Ravva, *Mater. Adv.*, 2022, **3**, 4954–4963.
25 T. Liu, X. Chen, J. Zhao, W. Wei, Z. Mao, W. Wu, S. Jiao, Y. Liu, Z. Yang and Z. Chi, *Chem. Sci.*, 2021, **12**, 5171–5176.
26 F. B. Dias, T. J. Penfold and A. P. Monkman, *Methods Appl. Fluoresc.*, 2017, **5**, 012001.
27 P. Schrögel, A. Tomkevičiene, P. Strohriegl, S. T. Hoffmann, A. Köhler and C. Lennartz, *J. Mater. Chem.*, 2011, **21**, 2266–2273.
28 M. Braune, M. Maiwald, B. Eppich, O. Brox, A. Ginolas, B. Sumpf and G. Tränkle, *IEEE Trans. Compon., Packag., Manuf. Technol.*, 2017, **7**, 720–725.
29 G. Li, X. Chen, Y. Chen and H. Jiang, *Opt. Lett.*, 2017, **42**, 939–942.
30 R. C. Eckardt, H. Masuda, Y. X. Fan and R. L. Byer, *IEEE J. Quantum Electron.*, 1990, **26**, 922–933.
31 Y. Xie, F. Liang, B. Zhang, B. Ge, H. Yu, Z. Lin, Z. Wang, H. Zhang, B. Huang and J. Wang, *ACS Omega*, 2019, **4**, 1045–1052.
32 S. F. Li, X. M. Jiang, Y. H. Fan, B. W. Liu, H. Y. Zeng and G. C. Guo, *Chem. Sci.*, 2018, **9**, 5700–5708.
33 I. Abdelwahab, G. Grinblat, K. Leng, Y. Li, X. Chi, A. Rusydi, S. A. Maier and K. P. Loh, *ACS Nano*, 2018, **12**, 644–650.
34 S. Maqbool, Z. Thekkayil and P. Mandal, *Adv. Opt. Mater.*, 2023, **11**, 2202942.
35 S. Maqbool, T. Sheikh, Z. Thekkayil, S. Deswal, R. Boomishankar, A. Nag and P. Mandal, *J. Phys. Chem. C*, 2021, **125**, 22674–22683.
36 E. W. Meijer, E. E. Havinga and G. L. J. A. Rikken, *Phys. Rev. Lett.*, 1990, **65**, 37.
37 A. Chaturvedi, P. K. Rajput, S. Maqbool, A. Nag and P. Mandal, *Adv. Mater.*, 2025, 2501022.
38 V. Nalla, R. Medishetty, Y. Wang, Z. Bai, H. Sun, J. Wei and J. J. Vittal, *IUCrJ*, 2015, **2**, 317–321.
39 Y. Yao, H. L. Xu and Z. M. Su, *J. Mater. Chem. C*, 2022, **10**, 886–898.
40 J. T. Ye, H. Q. Wang, Y. Zhang and Y. Q. Qiu, *J. Phys. Chem. C*, 2020, **124**, 921–931.
41 X. Yan, H. Peng, Y. Xiang, J. Wang, L. Yu, Y. Tao, H. Li, W. Huang, R. Chen, X. Yan, H. Peng, Y. Xiang, J. Wang, L. Yu, Y. Tao, H. Li, W. Huang and R. Chen, *Small*, 2022, **18**, 2104073.
42 S. Sahoo, N. Deka, R. Panday and R. Boomishankar, *Chem. Commun.*, 2024, **60**, 11655–11672.